

1 **Dominant Anomaly Patterns in the Near-Surface Baroclinicity and**
2 **Accompanying Anomalies in the Atmosphere and Oceans. Part II: North**
3 **Pacific Basin**

4 Mototaka Nakamura^a and Shozo Yamane^a

5 ^a*Japan Agency for Marine-Earth Science and Technology, Yokohama, Kanagawa, Japan*

6 *Corresponding author:* Mototaka Nakamura, moto@jamstec.go.jp

7 Shozo Yamane's current affiliation: Science and Engineering, Doshisha University, Kyotanabe,
8 Kyoto, Japan.

9 ABSTRACT: Variability in the monthly-mean flow and storm track in the North Pacific basin is
10 examined with a focus on the near-surface baroclinicity. Dominant patterns of anomalous near-
11 surface baroclinicity found from EOF analyses generally show mixed patterns of shift and changes
12 in the strength of near-surface baroclinicity. Composited anomalies in the monthly-mean wind
13 at various pressure levels based on the signals in the EOFs show accompanying anomalies in the
14 mean flow up to 50 hPa in the winter and up to 100 hPa in other seasons. Anomalous eddy
15 fields accompanying the anomalous near-surface baroclinicity patterns exhibit, broadly speaking,
16 structures anticipated from simple linear theories of baroclinic instability, and suggest a tendency
17 for anomalous wave fluxes to accelerate–decelerate the surface westerly accordingly. However,
18 the relationship between anomalous eddy fields and anomalous near-surface baroclinicity in the
19 midwinter is not consistent with the simple linear baroclinic instability theories. Composited
20 anomalous SST accompanying anomalous near-surface baroclinicity often exhibits moderate values
21 and large spatial scales in the basin, rather than large values concentrated near the oceanic fronts. In
22 the midsummer and in some cases in cold months, however, large SST anomalies are found around
23 the Kuroshio–Oyashio Extensions. Accompanying anomalies in the net surface heat flux, SST in
24 the preceding and following months, and meridional eddy heat flux in the lower troposphere suggest
25 active roles played by the ocean in generating the concomitant anomalous large-scale atmospheric
26 state in some of these cases.

²⁷ SIGNIFICANCE STATEMENT: Enter significance statement here, no more than 120
²⁸ words. See www.ametsoc.org/index.cfm/ams/publications/author-information/significance-statements/ for details.
²⁹

³⁰ **1. Introduction**

³¹ It has now become our basic knowledge that the extratropical atmosphere is driven strongly by the
³² horizontal potential temperature gradient that arises from the differential solar heating (e.g., Lorenz
³³ 1955). The horizontal gradient in the potential temperature, often referred to as baroclinicity, is a
³⁴ measure of upper-level wind steering via thermal wind and a measure of baroclinic instability in
³⁵ the atmosphere. Baroclinicity in the lower atmosphere in classic theories of atmospheric stability
³⁶ is measured by a combination of the static stability and horizontal temperature gradient, the latter
³⁷ of which is equivalent to vertical shear in the horizontal wind through the thermal wind balance
³⁸ (Charney 1947; Eady 1949). In its original form, the Eady's maximum growth rate for baroclinic
³⁹ instability B_{GRMax} is defined by $B_{GRMax} = 0.31(|f|/N)(\partial U/\partial z)$ in a zonally homogeneous steady
⁴⁰ mean state, where U is the mean zonal flow, f is the Coriolis parameter, and N is the Brunt–Väisälä
⁴¹ frequency. Charney's formula is slightly different from the Eady's, but still incorporates the same
⁴² effects (Table 1).

Month	EOF1	Split	EOF2	Split	EOF3	EOF4
Jan	29	NG	24	GD	10	5
Feb	39	GD	20	GD	7	6
Mar	31	GD	14	NG	10	6
Apr	23	GD	14	NG	10	7
May	19	GD	12	NG	10	7
Jun	19	GD	12	NG	10	9
Jul	18	NG	13	NG	9	7
Aug	18	NG	13	NG	11	9
Sep	17	NG	13	NG	10	8
Oct	16	NG	13	GD	8	7
Nov	19	NG	16	NG	11	8
Dec	33	GD	18	GD	10	6

⁴³ TABLE 1. Percentage of variance explained by the first four EOFs for the North Pacific Bx. The degree of
⁴⁴ separation between EOF1 and EOF2 and EOF2 and EOF3, based on the North et al. (1982) criterion, is indicated
⁴⁵ by good (GD) and not good or marginal (NG).

46 Lindzen and Farrell (1980) first applied the Eady's parameter to atmospheric data to successfully
47 estimate the maximum growth rate of baroclinic instability in the troposphere. Hoskins and Valdes
48 (1990) used its localized version (i.e., U , N , and f are all local Eulerian mean values) as the
49 central parameter in their study of the Northern Hemispheric storm tracks. This local version, or
50 its simplified version, has been used successfully as an indicator of baroclinic wave generation in
51 diagnostic studies of stormtracks in recent years as well (Nakamura and Sampe 2002; Nakamura
52 and Shimpo 2004; Nakamura et al. 2004). In our study, the North Atlantic part of which was
53 reported in Nakamura and Yamane (2009, hereafter Part I), we define the near-surface baroclinic
54 vector, $\mathbf{B} = B^x \mathbf{i} + B^y \mathbf{j}$, where $B^x = -(g/\theta N)(\partial\theta/\partial y)$ and $B^y = (g/\theta N)(\partial\theta/\partial x)$ with θ being the
55 monthly-mean potential temperature at 2 m above the surface, and use it as the central quantity
56 of the diagnoses. Unless stated otherwise, “anomalies” refer to deviations from the climatology
57 hereafter. Though its meridional component does not appear in any classic theory of baroclinic
58 instability, a theory that does incorporate the effect of B^y shows its important role in enhancing
59 baroclinic wave generation locally to the east of the mean trough (Niehaus 1980). In the North
60 Atlantic storm track region, we indeed found that the substantial zonal gradient in the surface
61 temperature in and around the Labrador Sea plays a major role in the large-scale atmospheric state.

62 2. The sea surface temperature

63 The sea surface temperature (SST) is an important factor in determining \mathbf{B} in the storm-track
64 regions (e.g., Hoskins and Valdes 1990; Nakamura et al. 2004; Part I). SST anomalies (SSTAs)
65 around an oceanic front along the Gulf Stream (GS), Kuroshio Extension (KE), or Oyashio Exten-
66 sion (OE) can have a profound impact on \mathbf{B} along the storm tracks.

67 a. A subtle point

68 A subtle but important point that has to be considered carefully in this regard is the spatial
69 scale and the location of SSTAs with respect to the climatology, since it is the anomalous surface
70 temperature gradient whose structure has a spatial scale of the atmospheric Rossby deformation
71 radius that can exert significant influence on the large-scale atmospheric flow.

72 1) CHANGES IN THE TEMPERATURE

73 The high sensitivity of **B** to changes in the temperature contrast across the front and changes
74 in the width of the front, and the uncertainty in the impact of SSTAs of small spatial scales on
75 **B** make it difficult to assess the effective **B** anomalies that are attributable to the SSTAs from the
76 available data. Moreover, it is uncertain exactly how the SSTAs in the presence or absence of the
77 land surface temperature anomalies may or may not produce **B** anomalies that are significant to the
78 atmosphere.

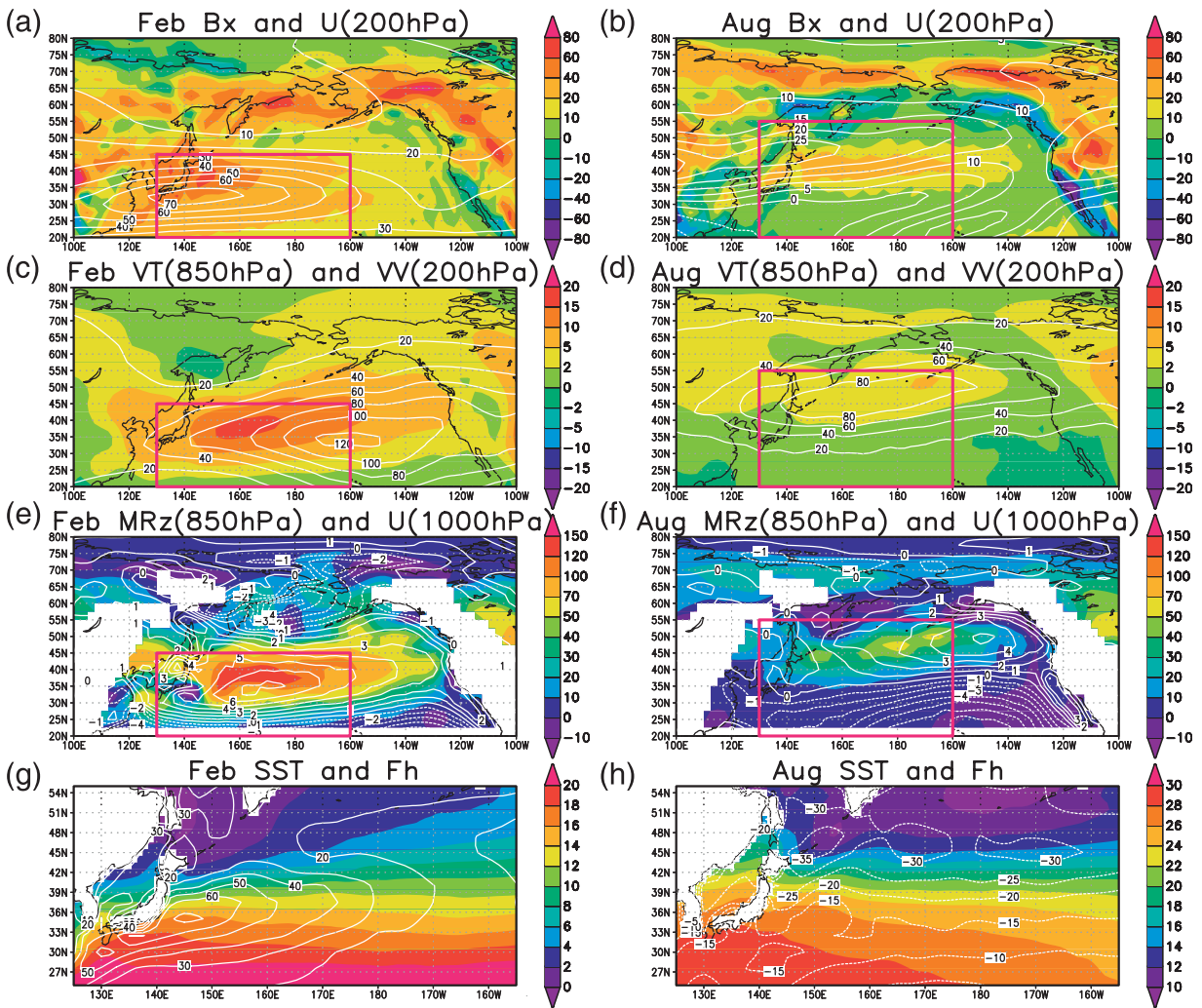
79 (i) *Complicating factor* The complicating factor introduced by the land surface must be taken
80 into account when studying potential roles of extratropical SSTAs in the extratropical atmospheric
81 anomalies.

82 Lau (1988) investigated patterns of anomalous storm track activity and associated low-frequency
83 flow anomalies by computing empirical orthogonal functions (EOFs) for high-frequency 500-hPa
84 geopotential height for the Northern Hemisphere winters. He found that both North Atlantic and
85 North Pacific storm tracks have a pattern of meridional shift and a pattern of increased or decreased
86 eddy activity in the first two EOFs. He also found that these changes in the storm tracks have
87 symbiotic relationships with the background flows and have substantial impacts on the mean flow.
88 Part I approached the issue of the stormtrack and low-frequency flow variability in connection with
89 SSTAs in the extratropics, focusing on **B** as the key parameter of diagnoses, and found similar
90 patterns of variability in the eddy activity and low-frequency flow in the North Atlantic basin. Much
91 of this variability was connected to SSTAs in the vicinity of the Gulf Stream in cold months (Part
92 I). Since the winter North Pacific basin has a storm track andmean flow that appear to be related
93 to the oceanic fronts, Kuroshio–Oyashio Extensions (KOE) in this case, in a manner essentially
94 the same as those in the North Atlantic basin related to the GS,we have attempted to find similar
95 results for the North Pacific basin. In this regard, we have chosen not to project our results onto
96 the major mode of variability in the extratropical North Pacific basin, the North Pacific decadal
97 variability (PDV), so that our presentation and discussion are mostly confined to the wave–mean
98 flow dynamics of monthly time scale or shorter.

99 Our approach to the search for a link between anomalies in the KOE and the overlying atmosphere
100 is as follows: (i) identify dominant patterns in anomalous **B** in the storm track for each calendar-
101 month and identify years in which the anomaly fits the pattern well, (ii) composite anomalies in

the monthly-mean circulation and highfrequency transients in the atmosphere to obtain a typical atmospheric state that accompanies the patterns of anomalous **B**, (iii) composite SSTA to obtain a typical oceanic state that accompanies and precedes the patterns of anomalous **B**, and (iv) composite anomalous net surface heat flux that accompanies and precedes the pattern of anomalous **B**. With this approach, we obtain typical pictures of anomalous states in the atmosphere and oceans with anomalous **B** as their connecting interface. Section 2 describes the data and procedure to compute **B**. Section 3 describes the climatology and variance of **B**. Dominant patterns of **B** are shown in section 4, followed by composited anomalies in various atmospheric fields and SST in section 5. Finally, we present our discussion on the results, examining a potential cause–effect relationship between anomalies in the SST and atmosphere in section 6.

Figure 1 shows the climatology of B_x , U^{200} , $\overline{V'\theta'}^{850}$, $\overline{V'\theta'}^{200}$, MR^{z850} , U^{1000} , SST, and F_h for February and August as examples of the reference state in the winter and summer. The numeric superscript indicates the pressure level in hPa. The seasonal mean is visibly more diffused in structure, particularly for B_x , than those shown in Fig. 1. There are no surprises in the overall picture of B_x . The regions of large land–sea temperature contrast and the oceanic fronts show very large B_x in cold months. The position of B_x maximum in the storm track region is found along the KOEregion throughout the year. The zonally elongated band of large B_x in the storm track is generally wider in cold months than in warm months. In fact, large B_x values that presumably accompany the Kuroshio and its extension in the cold months vanish in the summer (Figs. 1a,b). The seasonal variation in the B_x values in the storm track basically follows that of the north–south differential heating—largest in the winter and smallest in the summer. As reported by Nakamura et al. (2004), the U^{200} maximum is displaced southward from the B_x maximum visibly in winter months (Fig. 2a), although U^{200} is generally large over the area of large B_x in the core of the storm track. The southward displacement of the U^{200} maximum from the B_x maximum in the storm track is less pronounced or even reversed in warmer months (Fig. 2b). We note that the structure of the climatological B_x generally reflects those of $(\partial\theta^{2m}/\partial y)$ with some exceptions where the surface slope contributes significantly to B_x in isolated areas over the land, most notably around the Himalayas.



112 FIG. 1. Climatology of B_x ($10^{-6} s^{-1}$, color) and U^{200} ($m s^{-1}$, contours) for (a) February and (b) August;
 113 $\overline{V'\theta'}^{850}$ ($K m s^{-1}$, color) and $\overline{V'V'}^{200}$ ($m^2 s^{-1}$, contours) for (c) February and (d) August; MRz^{850} ($10^{-3} m^2 s^{-2}$,
 114 color) and U^{1000} ($m s^{-1}$, contours) for (e) February and (f) August; and SST (K, color) and F_h [$10^5 J m^{-2} (6$
 115 $h)^{-1}$] for (g) February and (h) August. Red rectangles indicate the domain of EOF calculations.

134 The position and structure of the storm track as indicated by $\overline{V'\theta'}^{850}$ and $\overline{V'V'}^{200}$ are, at least for
 135 the winter, essentially the same as those reported in earlier studies on the storm tracks (e.g., Chang
 136 et al. 2002). The maxima in $\overline{V'\theta'}^{850}$ and $\overline{V'V'}^{200}$ are located in the band of large B_x .

137 3. Data and calculation procedures

138 The data used to calculate \mathbf{B} are the monthly-mean temperature at 2 m above the surface (T^{2m})
 139 and temperature at pressure levels available from the 40-yr European Centre for Medium-Range

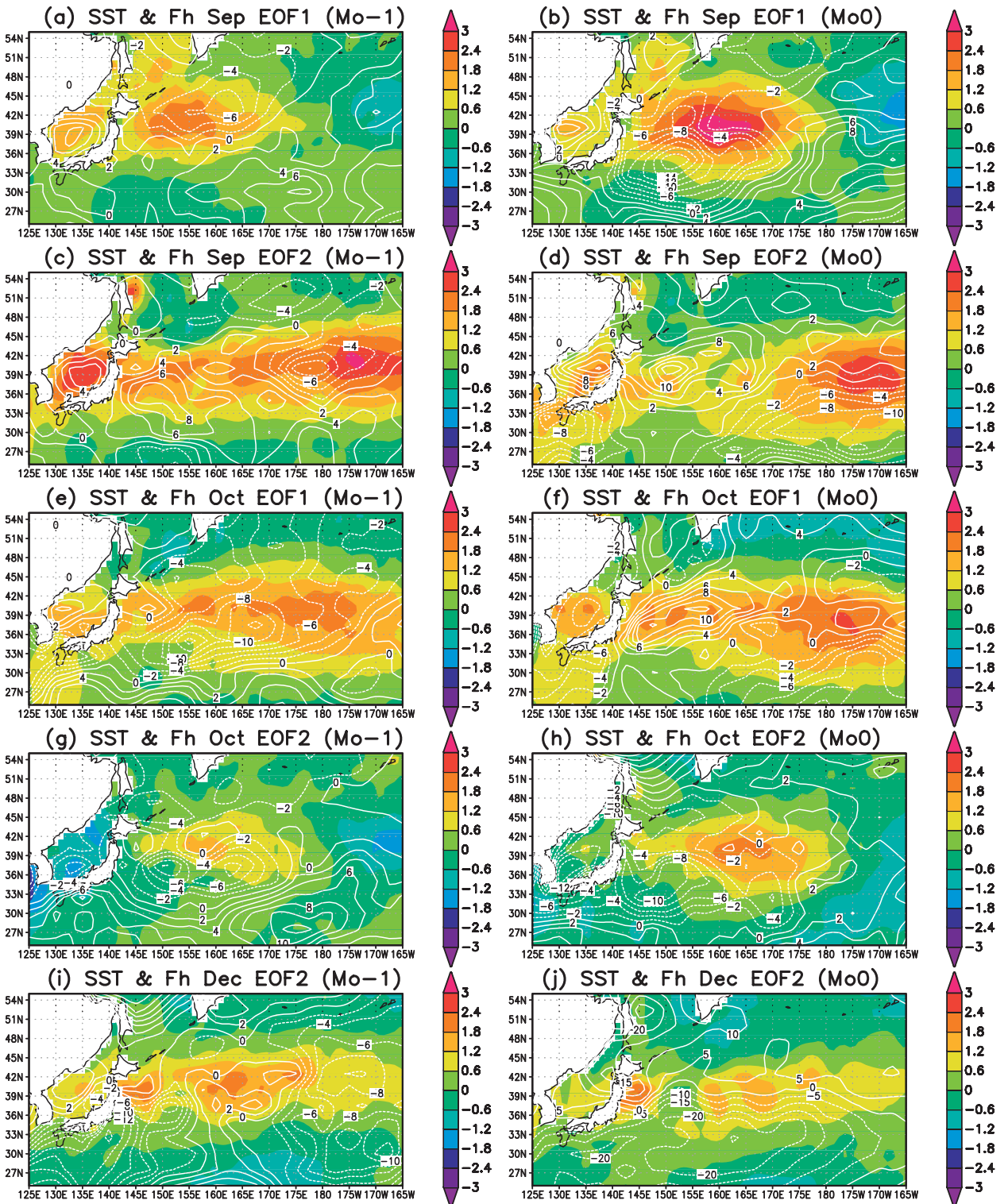


FIG. 2. As in Fig. 10, but for (a),(b) September EOF1; (c),(d) September EOF2; (e),(f) October EOF1; (g),(h) October EOF2; and (i),(j) December EOF2.

140 Weather Forecasts (ECMWF) Re-Analysis (ERA-40; Uppala et al. 2005). We chose the ERA-
141 40 T^{2m} data rather than the National Centers for Environmental Prediction–National Center for
142 Atmospheric Research (NCEP–NCAR) reanalysis products for its explicit inclusion of the observed
143 near-surface temperature in producing the T^{2m} data. The monthly-mean surface pressure data from
144 the NCEP–NCAR reanalyses (Kalnay et al. 1996) were used to determine the pressure levels to
145 be used for **B** calculation, and to calculate θ at 2 m above the surface from T^{2m} . We used the
146 NCEP–NCAR surface pressure data for convenience, since we had already compiled the dataset for
147 calculating transient eddy fluxes to be mentioned later and the ERA-40 surface pressure data are
148 not readily available. We later compared the NCEP–NCAR monthly-mean sea level pressure with
149 that of ERA-40, and found the difference between the two products to be immaterial for the purpose
150 of the current study. We also used ERA-40 monthly-mean horizontal wind and geopotential height
151 at pressure levels, net surface heat flux, Fh (the sum of latent heat flux, sensible heat flux, solar
152 radiation, and the thermal radiation), and Hadley Centre sea surface temperature data (Rayner et
153 al. 2003) to compile anomaly composites accompanying anomalous patterns in **B**. In addition, we
154 used 6-hourly temperature and wind data from the NCEP–NCAR reanalyses to compute various
155 eddy fields. The accuracy of the Fh data used here is, as true for other reanalyses surface heat flux
156 products, may not be so high to produce reliable anomaly composites.

157 We computed **B** near the surface by calculating the horizontal gradient in θ^{2m} , using the centered
158 finite differencing, and calculating N from the lowest three vertical pressure levels that are location
159 dependent because of topography. Both $\nabla\theta^{2m}$ and N were calculated locally as in Hoskins and
160 Valdes (1990) and Nakamura and Shimpo (2004). The entire 45 yr from September 1957 to August
161 2002 were used for the Northern Hemisphere. To resolve the dominant modes in **B** arising from
162 the land–sea temperature contrast, one may need much higher horizontal resolution in the data.
163 The relatively coarse horizontal resolution of the data may artificially suppress the significance of
164 the variability associated with the land–sea temperature contrast. One should keep this limitation in
165 mind. The 6-hourly bandpassed (period of 2–7 days) eddy fields and ultra-low-frequency (period
166 of 30 days and longer) background fields were computed from the NCEP– NCAR reanalyses, using
167 simple time filters (Lau and Lau 1984) first. The filtered time series were then visually examined
168 against the raw time series and, then, used to calculate the slowly evolving bandpassed meridional
169 velocity variance ($\overline{V'V'}$), meridional temperature flux ($\overline{V'\theta'}$), and the three-dimensional transient

wave activity flux defined on a zonally varying basic state by Plumb (1986). The wave activity flux consists of the zonal and meridional advective fluxes (MU and MV), the zonal and meridional radiative fluxes (MR_x and MR_y), and the radiative vertical flux (MR_z). The flux is essentially the Eliassen–Palm flux (Eliassen and Palm 1961) in a zonally inhomogeneous mean flow (Plumb 1986). The wave activity flux was calculated from February 1948 to November 2004 only for the extratropics poleward of 20° latitude. Also, it was calculated only from 850 to 30 hPa because of the double differentiation with respect to pressure required for the calculation. The flux of particular interest in this study is the vertical component. Here MR_z is defined by

$$MR^z = \frac{pf \cos \phi}{p^0 |\nabla h\bar{q}|(d\theta_0/dz)} \left(\frac{\partial \bar{q}}{\partial x} \overline{U' \theta'} + \frac{\partial \bar{q}}{\partial y} \overline{V' \theta'} \right),$$

where q is quasigeostrophic potential vorticity, p is the pressure, p^0 is the reference surface pressure set to 1000 hPa here, θ_0 is the area-weighted ultra-low-frequency hemispheric mean potential temperature at each height, u_9 is the bandpassed potential temperature, and z is the geopotential height. An overbar denotes an ultra-low frequency component and a prime denotes bandpassed component. The 6-hourly time series of wave fluxes was computed by using the time series of ultra-low-frequency fields as the basic-state and high-frequency fields as eddies. In short, the time series was calculated by changing the meaning of an overbar from the time mean state to an ultra-low-frequency state, and changing the meaning of a prime from a departure from the mean to a high-frequency state. The 6-hourly eddy time series was averaged over each month to produce monthly-mean time series. This dataset allows us to examine anomalous eddy fields accompanying anomalous \mathbf{B} in specific months. The climatology for the eddy fields was computed from 46 yr, January 1958 to December 2003. The calculation of the wave activity and its flux is described in detail by Nakamura et al. (2010).

4. Climatology and variance

The climatology and variance of B_x and B_y were computed for each calendar month and examined closely for their spatial and temporal structures. The monthly climatology, rather than the seasonal climatology, is used as the reference in our study, to avoid contamination of the diagnostic results arising from differences in the climatology between two successive months. Unlike in the North Atlantic basin reported in Part I, we found the impact of B_y variations on the

¹⁹⁷ large-scale atmospheric state in the North Pacific basin much weaker than that of B_x variations,
¹⁹⁸ presumably because of the more zonal orientation of the KOE in comparison to the Gulf Stream
¹⁹⁹ and North Atlantic Current. In the following, thus, we focus our presentation on the climatology
²⁰⁰ and variations of B_x and their impact on the large-scale atmospheric state.

²⁰¹ Sample citations: Becker and Schmitz (2003), Knutti et al. (2008), and (Meixner et al. 2002;
²⁰² Kuji and Nakajima 2002; Emery et al. 1986).

203 *Acknowledgments.* We thank two anonymous reviewers for their comments, which helped to
204 improve the manuscript.

205 *Data availability statement.* Start data availability statement here.

206 APPENDIX A

207 **Appendix Title**

208 *Appendix section head*

209 Here is a sample appendix with an equation [see Eq. (A1)]. Lorem ipsum dolor sit amet,
210 consectetur adipiscing elit, sed do eiusmod tempor incididunt ut labore et dolore magna aliqua. Ut
211 enim ad minim veniam, quis nostrud exercitation ullamco laboris nisi ut aliquip ex ea commodo
212 consequat.

$$\frac{pf \cos \phi}{p^0 |\nabla h\bar{q}|(d\theta_0/dz)} \quad (\text{A1})$$

213 Lorem ipsum dolor sit amet, consectetur adipiscing elit, sed do eiusmod tempor incididunt ut
214 labore et dolore magna aliqua. Ut enim ad minim veniam, quis nostrud exercitation ullamco laboris
215 nisi ut aliquip ex ea commodo consequat. Duis aute irure dolor in reprehenderit in voluptate velit
216 esse cillum dolore eu fugiat nulla pariatur. Excepteur sint occaecat cupidatat non proident, sunt in
217 culpa qui officia deserunt mollit anim id est laborum.

218 Lorem ipsum dolor sit amet, consectetur adipiscing elit, sed do eiusmod tempor incididunt ut
219 labore et dolore magna aliqua. Ut enim ad minim veniam, quis nostrud exercitation ullamco laboris
220 nisi ut aliquip ex ea commodo consequat. Here is an example appendix figure (see Fig. A1).

221 APPENDIX B

222 **Second Appendix Title**

223 *a. Sample appendix section head*

224 Lorem ipsum dolor sit amet, consectetur adipiscing elit, sed do eiusmod tempor incididunt ut
225 labore et dolore magna aliqua. Ut enim ad minim veniam, quis nostrud exercitation ullamco laboris
226 nisi ut aliquip ex ea commodo consequat [see Eq. (B1)]. Duis aute irure dolor in reprehenderit

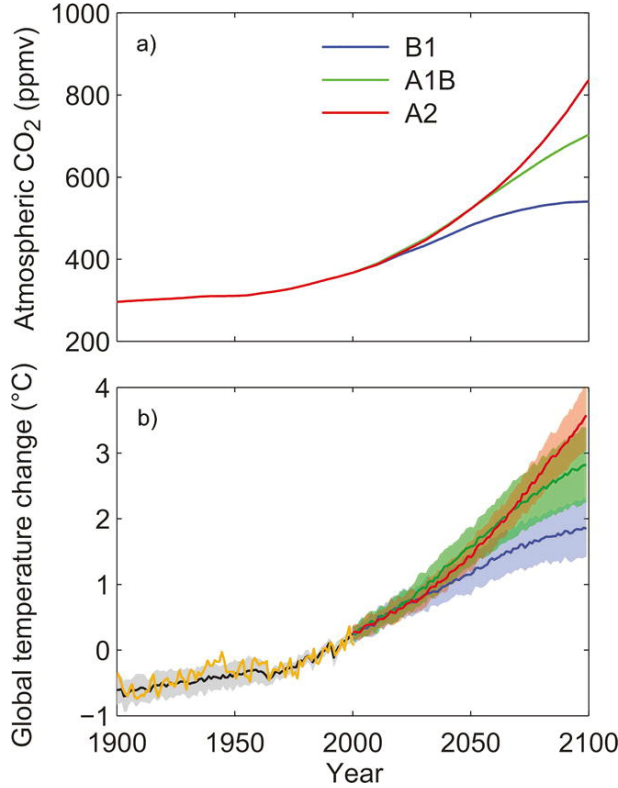


FIG. A1. Here is an appendix, single column figure caption.

227 in voluptate velit esse cillum dolore eu fugiat nulla pariatur. Excepteur sint occaecat cupidatat non
 228 proident, sunt in culpa qui officia deserunt mollit anim id est laborum.

$$\left(\frac{\partial \bar{q}}{\partial x} \overline{U' \theta'} + \frac{\partial \bar{q}}{\partial y} \overline{V' \theta'} \right) \quad (\text{B1})$$

229 Lorem ipsum dolor sit amet, consectetur adipiscing elit, sed do eiusmod tempor incididunt ut labore
 230 et dolore magna aliqua. Ut enim ad minim veniam, quis nostrud exercitation ullamco laboris nisi
 231 ut aliquip ex ea commodo consequat. Duis aute irure dolor in reprehenderit in voluptate velit esse
 232 cillum dolore eu fugiat nulla pariatur. Excepteur sint occaecat cupidatat non proident, sunt in culpa
 233 qui officia deserunt mollit anim id est laborum. Lorem ipsum dolor sit amet, consectetur adipiscing
 234 elit, sed do eiusmod tempor incididunt ut labore et dolore magna aliqua. Ut enim ad minim veniam,
 235 quis nostrud exercitation ullamco laboris nisi ut aliquip ex ea commodo consequat. Duis aute irure
 236 dolor in reprehenderit in voluptate velit esse cillum dolore eu fugiat nulla pariatur. Excepteur sint
 237 occaecat cupidatat non proident, sunt in culpa qui officia deserunt mollit anim id est laborum.

238 b. Sample appendix section head

239 Second appendix example. Here an example appendix table (see Table B1).

Month	Yr of positive phase
Jan	1961, 1969, 1978, 1979, 1988, 1990, 1992, 1994
Feb	1964, 1977, 1978, 1980, 1983, 1986, 1988, 2000, 2001
Mar	1970, 1973, 1979, 1980, 1984, 1988, 2000
Apr	1959, 1961, 1962, 1963, 1968, 1972, 1983, 2002
May	1971, 1984, 1993, 1996, 2000
Jun	1981, 1983, 1984, 1993, 1998
Jul	1961, 1972, 1973, 1978, 1994, 2000
Aug	1967, 1970, 1973, 1978, 1994, 1999
Sep	1975, 1977, 1988, 1989, 1994, 1998, 1999
Oct	1962, 1977, 1998, 1999, 2001
Nov	1985, 1986, 1987, 1988, 1991, 1998
Dec	1957, 1968, 1972, 1978, 1979, 1990

TABLE B1. Years selected for anomaly composites for the positive phase of B^x EOF1.

240 **References**

- 241 Becker, E., and G. Schmitz, 2003: Climatological effects of orography and land–sea heating
242 contrasts on the gravity wave–driven circulation of the mesosphere. *J. Atmos. Sci.*, **60**, 103–118,
243 [https://doi.org/10.1175/1520-0469\(2003\)060<0103:CEOAL>2.0.CO;2](https://doi.org/10.1175/1520-0469(2003)060<0103:CEOAL>2.0.CO;2).
- 244 Emery, W. J., A. C. Thomas, M. J. Collins, W. R. Crawford, and D. L. Mackas, 1986: An objective
245 method for computing advective surface velocities from sequential infrared satellite images. *J.*
246 *Geophys. Res.*, **91**, 12 865–12 878, <https://doi.org/10.1029/JC091iC11p12865>.
- 247 Knutti, R., and Coauthors, 2008: A review of uncertainties in global temperature projections over
248 the twenty-first century. *J. Climate*, **21**, 2651–2663, <https://doi.org/10.1175/2007JCLI2119.1>.
- 249 Kuji, M., and T. Nakajima, 2002: Retrieval of cloud geometrical parameters using remote sensing
250 data. *11th Conf. on Cloud Physics*, Ogden, UT, Amer. Meteor. Soc., JP1.7, <http://ams.confex.com/ams/pdfpapers/39550.pdf>.
- 252 Meixner, T., L. A. Bastidas, H. V. Gupta, and R. C. Bales, 2002: Multicriteria parameter estimation
253 for models of stream chemical composition. *Water Resour. Res.*, **38**, 1027, <https://doi.org/10.1029/2000WR000112>.